A Proposal for Discrete Modeling of Mechanical Effects During Drying, Combining Pore Networks With DEM

Abdolreza Kharaghani, Thomas Metzger, and Evangelos Tsotsas
Thermal Process Engineering, Otto von Guericke University, P.O. 4120, 39016 Magdeburg, Germany

DOI 10.1002/aic.12318
Published online July 13, 2010 in Wiley Online Library (wileyonlinelibrary.com).

A discrete modeling approach is introduced to investigate the influence of liquid phase distributions on damage and deformation of particle aggregates during convective drying. The approach is illustrated on a simple 3D aggregate structure, in which monosized spherical particles are arranged in a cubic packing and bonded together at their contacts; the mechanical behavior of this aggregate is simulated by discrete element method (DEM). Liquid phase distributions in the void space are obtained from drying simulations for a pore network. In a one-way coupling approach, capillary forces are computed over time from the filling state of pores and applied as loads on each particle in DEM. A nonlinear bond model is used to compute interparticular forces. Simulations are conducted for various drying conditions and for aggregates with different mechanical properties. Microcracks induced by bond breakage are observed in stiff material, whereas soft material tends to shrink reversibly without damage. © 2010 American Institute of Chemical Engineers *AIChE J,* 57: 872–885, 2011
Keywords: pore network modeling, discrete element method, multiphase, microcracks, shrinkage

Introduction

Drying is undeniably a complex process involving various transport processes, such as two-phase flow with liquid-vapor phase change, which are accompanied by undesired mechanical effects. These effects—widely encountered, but poorly understood—are a major problem in drying industry and present a challenge for modeling and simulation of drying. Therefore, a profound study is essential to learn about the fundamental reasons of these effects and to find ways to control them, to analyze them, and to develop, as the result of such analysis, methods and conditions of drying, which would lead not only to a preservation of the quality of the dried material but also to its improvement. It is known that convective-drying induced mechanical effects mainly depend upon moisture distribution, which is influenced by drying conditions and the porous material itself. As major aspects, a theoretical investigation should consider structural and mechanical properties of the solid as well as the mechanisms controlling liquid flow (mainly capillary and viscous effects) that depend on process parameters.

Several approaches in this sense have been taken in literature. Lewis et al.[1] coupled classical heat and mass transfer equations with an elastic constitutive model to find drying-induced stresses in capillary porous bodies. A thermomechanical approach to shrinkage and cracking phenomena in drying, which is based on thermodynamics of irreversible processes and continuum mechanics of porous media, was proposed by Kowalski.[2] X-ray microtomography was used to monitor shrinkage and cracks of drying organic gels under different drying conditions.[3] Recently, simulated drying stresses were compared with measured tensile strength to

Correspondence concerning this article should be addressed to T. Metzger at thomas.metzger@ovgu.de.

give a criterion for crack initiation.[4] In this work, the first crack appears at the point where the strength curve crosses the simulated tensile stress curve. Different strategies are used in literature[5] to model shrinkage during drying. In these works, the partially saturated porous medium is treated as a fictitious continuum and coupling between the transfer processes and mechanical interactions are considered as follows. First, fundamental balance equations together with phenomenological rate equations for heat and mass transfer—involving effective parameters, which themselves depend on one or more physically independent variables—are solved by use of traditional numerical techniques to obtain time-dependent temperature and moisture content distributions. Then, depending on the drying period and material itself, rheological behaviors, such as elasticity, viscoelasticity, and plasticity, are applied to model mechanical effects that appear in drying. Despite the strengths and extensive applications of these models, they are phenomenological and primarily concerned with mathematical modeling of the observed phenomena without detailed attention to pore-scale physics, such as transport phenomena and direct interactions between solid and liquid phase.

As a more fundamental approach to drying, pore network models (PNMs) have more recently been adopted by scientists. In these models, the porous medium is represented by a network of interconnected pores, which have a prescribed geometry but are random in their size; and pore-scale transport phenomena for each phase are described explicitly. This ensures that effects are not lost or masked during up-scaling to the product scale. So far, investigations with PNMs have predominately considered the influence of physical effects and structural properties on drying kinetics. Concerning physical effects, viscosity is either completely neglected[6] or accounted for in liquid phase[7] or in both liquid and gas phase.[8] A stabilization of the drying front has been observed by considering gravity and liquid viscosity.[9,10] Further model extensions include film effects[11,12] and heat transfer.[13–15] Apart from physical effects, some studies focus on the influence of structural properties, such as pore shape[12,16] and pore size distribution (mono- and bimodal), spatial correlation of pore size, and coordination number of the regular network.[17]

Few notable works have been published on the understanding of mechanical effects arising during drying from pore level effects. Brinker and Scherer[18] have done comprehensive investigations on the driving forces causing shrinkage and cracks during drying of gels. Surface deformation of solids has also been analyzed as due to capillary forces.[19] Recently, numerical drying curves have been studied to see the influence of shrinkage for a network of pores whose radii are reduced with increasing capillary pressure.[20] In the above-mentioned work, driving force for cracking and shrinkage is understood, but never modeled at the microlevel. This work sets out to explore these effects by means of discrete networks of pores and particles, respectively.

In spite of significant advances in pore network drying models, there are still open issues. For instance, these network models do not include solid phase geometry explicitly. Therefore, local effects on solid phase (such as cracks) can not be described. In principle, these effects are due to capillary forces, which induce stresses on the solid phase causing displacement. This work sets out to explicitly model the solid phase in the case that the porous material can be reasonably represented by a network of spherical particles, such as particle aggregates obtained by sintering, sol-gel processing, or agglomeration. Capillary forces obtained from a PNM are applied to these particles, and their mechanical response is computed by discrete element method (DEM).

DEM is an alternative to the classical continuum mechanics approach, which has originally been developed for rock mechanics. Unlike traditional numerical methods, this meshfree technique can treat the solid phase as an assembly of discrete elements, starting with basic constitutive laws at interparticle contacts and providing microscopic interactions of the particles and their contacts under different loading conditions. Indeed, such microscopic information not only can be significant for a better understanding of the phenomenon but also opens up possibilities for microstructural material design. However, computational requirements in DEM simulations are inevitably demanding, as the number of equations governing the system depends on the number of particles used to capture the microstructure, so that simulations are usually carried out on a limited number of spherical particles (instead of more complex particle geometries).

Initially, DEM has been widely used to model disaggregated media[21] that occur naturally, such as sand, rocks, and rock-falls. Recent work includes fundamental studies on breakage processes and strength of individual dry agglomerates[22,23] proving that DEM can be successfully applied to particle systems with solid bonds to describe their experimental cracking and breakage behavior. Furthermore, wet granular materials have been modeled,[24,25] in which capillary force has been expressed as a function of interparticle distance, water bridge volume, contact angle, and surface tension. To date little report of DEM application on drying has been found in literature.[26]

In this article, we propose a discrete approach to model and simulate the mechanical effects as a result of liquid phase evolution during convective drying of porous materials. The scope of this work is to explain the new simulation tool, demonstrate that it can describe relevant phenomena during drying at a qualitative level, and—on a simple example—illustrate what chances the numerical results offer regarding a microscale analysis of drying. Only future work will allow the model to become predictive, both by model development and parameterization in well-defined experiments.

The several assumptions that are made in this pioneering work have to be seen in this light that they are not inherent to the modeling approach, but can be disposed of by model extensions. Specifically, the considered particle aggregates are of cubic arrangement, for which the pore network is also cubic and local capillary forces are easily computed. Pore size, however, needs to be randomized to obtain the typical capillary effects. The generalization to irregular aggregate structures is possible; then, the pore network can be obtained, for example, by the use of a Voronoi method,[27] allowing for a natural computation of pore sizes and yielding a complementary pore network in a strict sense. Furthermore, heat transfer is not modeled, and macroscopic stresses because of liquid pressure gradients are not yet accounted for; both effects can be included as has been done for pure pore network modeling.

Supporting the isothermal model assumption, it shall be stressed that mechanical effects induced by moisture removal

are typically one or two orders of magnitude larger than effects solely caused by thermal expansion of the drying material.[2] Furthermore, temperature gradients in the liquid-filled pore regions are usually small for convective drying so that thermal effects on the phase distributions can be neglected.[13–15]

First, the pore network drying model of Prat, which has recently been extended concerning geometrical and physical aspects,[28] is recalled and governing structural and mass transport rules are paraphrased. Then, the DEM is briefly introduced and its assumptions and limitations are discussed. Further, the porous structure is encoded into discrete phases using pore network and DEM approaches. On this basis, a one-way coupling of pore and particle networks is introduced by describing capillary forces as a function of pore saturations. The model is consecutively applied to particle aggregates under different drying conditions. Two limiting cases are considered that can be interpreted as (1) slow and fast drying or as (2) two pore liquids with very different ratios of surface tension to viscosity. Simulation of the two cases leads to different capillary force distributions in the particle network. The respective mechanical response is captured by tracking contact forces and, for stiff aggregates, simulating and analyzing the resulting cracks. The influence of material properties on cracks formation is illustrated. For specific material properties, reversible shrinkage without cracks is obtained as observed experimentally as spring-back during drying of certain gels. We end with a summary of the main findings and mention potential works for the future.

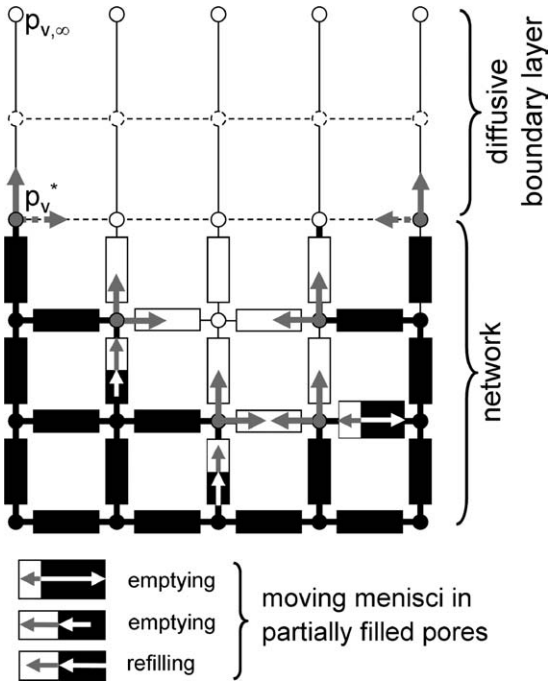

Figure 1. Partially saturated pore network including diffusive boundary layer.

Liquid pores and nodes are in black; gas ones in white; gray nodes are at saturation vapor pressure. Vapor diffusion is shown as gray arrows; its boundary conditions are illustrated. For partially filled pores, liquid flow is shown as white arrows.

Description of Pore Network Drying Model

The PNM is a modern discrete approach for the study of transport phenomena in porous media in general and of drying in particular. In this approach, the complicated pore space geometry is conceptualized by a network of nodes (standard is 2D square and 3D cubic), which are interconnected by cylindrical pores. Transport phenomena are described by using some local rules straightly at the pore level. The PNM used in our study was initiated in pioneering works by Prat, who elucidated the drying phenomenon as an invasion percolation driven by evaporation. In this work, we recall the isothermal PNM, which is based on the following elements and rules.

Data structure

The data structure describes the connectivity of the (cylindrical) pores and nodes in the network and its boundary layer. The conceptual model of a pore network is depicted in Figure 1. The network consists of pores of uniform length L, the radii r_{ij} of which are randomly assigned according to a probability density function; the saturation states of pores and nodes evolve during drying.

Mass transfer mechanisms

Mass transfer in the network is controlled by vapor diffusion in the gas-filled region and liquid flow in the liquid-filled part of the network by taking into account the following assumptions. Liquid films and adsorption are not modeled; porous media are considered as capillary with only free water and perfect wetting. Gravity deliberately is set to zero but could be included if larger pores and large objects shall be studied; and viscosity in gas phase is not modeled (reasonable for moderate drying conditions) so that gas pressure is constant. Both Kelvin and Knudsen effects are neglected. Initially, the network is completely saturated with water. Its top surface is open for evaporation, however, the bottom is closed and the other surfaces are impervious (see Figure 1). To compute the vapor diffusion, quasisteady balances for mass flow rates (in kg/s) are set up for any gas pore i by

$$\sum_j \dot{\mathrm{M}}_{v,ij} = \sum_j A_{ij} \frac{\delta}{L} \frac{p_g \tilde{\mathrm{M}}_v}{\tilde{R}T} \cdot \ln\left(\frac{p_g - p_{v,i}}{p_g - p_{v,j}}\right) = 0 \qquad (1)$$

(regardless of its position in the network or in the boundary layer) where L is distance between nodes, A_{ij} exchange area ($\pi {r_{ij}}^2$ for network, L^2 for boundary layer), δ vapor diffusivity, $\tilde{\mathrm{M}}_v$ molar vapor mass, $\tilde{\mathrm{R}}$ universal gas constant, p_g gas pressure, T temperature (in K) and $p_{v,i}$ vapor pressure (in Pa). The system of Eq. 1 is solved for unknown vapor pressures by applying the vapor pressure of drying air at the top edge of the boundary layer and saturation vapor pressure next to the gas-filled interface. In the liquid domain, if viscosity can be neglected, the following algorithm is implemented. (1) Every liquid cluster is identified. (2) According to the invasion percolation rule, the pore connected to the gas-invaded region, which has lowest capillary pressure is identified for each cluster. (3) The evaporation flux at the boundary of each

cluster is computed. (4) For each cluster, the mass loss corresponding to this evaporation flux is assigned to the invasion pore. (5) The pore of all clusters that empties first sets the time step as liquid connectivity as well as the set of Eq. 1 for vapor diffusion may change. (6) The phase distribution within the network is updated and the above-described procedure is repeated.

To compute liquid flow rates (in kg/s) if viscosity cannot be neglected, the mass balance in any liquid node is expressed by

$$\sum_j \dot{\mathrm{M}}_{w,ij} = \sum_j \frac{\pi r_{ij}^4}{8 v_w L_{ij}} \left(p_{w,i} - p_{w,j}\right) = 0 \tag{2}$$

where v_w is kinematic viscosity of water (in m^2/s) and L_{ij} liquid-filled length of pore. The linear system of Eq. 2 must be solved for unknown liquid pressures $p_{w,i}$. Boundary conditions to Eq. 2 are given at the liquid-gas interface. For a stationary meniscus, that is, where capillary pressure can provide liquid water at the local evaporation rate, the second type boundary condition $\dot{M}_{w,ij} = \dot{M}_{v,ij}$ is applied. For a moving meniscus, that is, where evaporation takes place at a higher rate than capillary flow (or for any partially filled pore), the boundary condition of first kind $p_{w,j} = p_g - 2\sigma/r_{ij}$ (with surface tension σ) is used. As boundary conditions on the flow problem depend on meniscus states themselves, an iterative procedure is used to find the states of the menisci.[10] For correct boundary conditions, the motion of menisci is obtained as the difference between evaporation flow rate and liquid flow rate. In the viscous case, several menisci per cluster may move. Depending on meniscus motion, pores may empty and partially saturated pores may refill again. Time stepping is imposed by the complete emptying (or refilling) of a meniscus pore; then, vapor and liquid flow problems must be solved for new boundary conditions.

DEM Formulation

The DEM is a numerical technique to study the mechanical behavior of complex systems, not only homogenous but also heterogeneous (in particle and bond properties), of discrete bodies or particles. They are mostly modeled as circular disks (2D) or spheres (3D) though they can also be arbitrarily shaped. The interaction between particles is described by applying the equations of motion to each particle, and a contact law to each inter-particle contact. The DEM used in this study was developed by Cundall,[29] who restricted himself to modeling of spherical particles, so that the numerical simulation is based on the following assumptions and rules:

- All particles are treated as undeformable balls.
- In (elastic) contacts, shape deformation of particles is not described explicitly, but represented by a virtual overlap (soft-contact approach).
- Overlap distance is related to contact force via the contact law; it is small as compared to particle size.

Linear contact law

The contact law relates the relative displacement of two particles at a contact to the contact force acting on them. Figure 2 shows a contact model by two particles at positions $\mathbf{x}_i$ and $\mathbf{x}_j$, with radii R_i and R_j, respectively. The unit normal vector $\mathbf{n}_{ij}$ (the suffix denotes the contact between particles i and j) is defined by

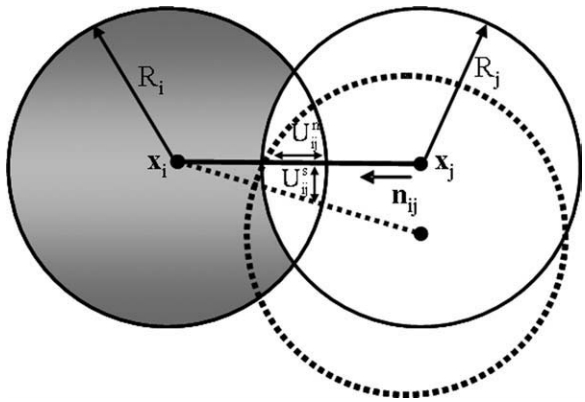

Figure 2. Interaction between two particles.

$$\mathbf{n}_{ij} = \frac{\mathbf{x}_j - \mathbf{x}_i}{d_{ij}}, \; d_{ij} = \left|\mathbf{x}_j - \mathbf{x}_i\right|. \tag{3}$$

The contact force vector $\mathbf{F}_{ij}$ can be resolved into normal and shear components with respect to the contact plane as

$$\mathbf{F}_{ij} = \mathbf{F}_{ij}^n + \mathbf{F}_{ij}^s. \tag{4}$$

The normal contact force vector is computed by

$$\mathbf{F}_{ij}^n = \mathrm{F}_{ij}^n \mathbf{n}_{ij} = \mathrm{K}_{ij}^n U_{ij}^n \mathbf{n}_{ij} \tag{5}$$

where K_{ij}^n is normal contact stiffness (in N/m) and $\mathrm{U}_{ij}^n = \mathrm{R}_i + \mathrm{R}_j - \mathrm{d}_{ij}$ normal overlap distance. The shear contact force is computed in an incremental fashion. When the contact is formed, the total shear contact force is initialized to zero. Each subsequent relative shear-displacement increment (resulting from a shear contact velocity $\mathbf{V}_{ij}^s$ for the numerical time step Δt)

$$\Delta \mathbf{U}_{ij}^s = \mathbf{V}_{ij}^s \Delta t \tag{6}$$

results in an increment of shear force

$$\Delta \mathbf{F}_{ij}^s = -\mathrm{K}_{ij}^s \Delta \mathbf{U}_{ij}^s \tag{7}$$

(with contact shear stiffness K_{ij}^s) that is added to the current value of contact shear force

$$\mathbf{F}_{ij}^s \leftarrow \mathbf{F}_{ij}^s + \Delta \mathbf{F}_{ij}^s. \tag{8}$$

To obtain realistic behavior and numerical stability, viscous damping needs to be added to the contact model.[21,30] Damping forces act in both normal and shear directions and are proportional to the respective contact velocities; the proportionality factor is $2\zeta\sqrt{\mathrm{K}_{ij} m_i m_j/(m_i + m_j)}$, where ζ is the damping ratio (see Table 2), m_i and m_j denote the particle masses and K_{ij} the contact stiffness.

It should be noted that for contacts between unbonded spherical particles, which experience small strain conditions and exclusively compressive stresses, the Hertz model is a more suitable contact law.[30] But, in the present case of

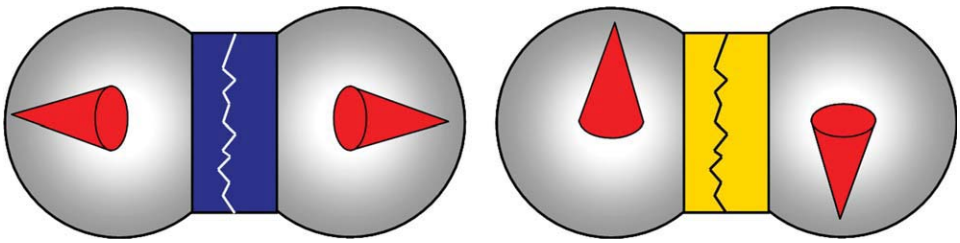

Figure 3. Schematic illustration of (external) forces on the particles (red cones) and resultant cracks of the parallel bond, normal (in dark blue) or shear (in yellow).

[Color figure can be viewed in the online issue, which is available at wileyonlinelibrary.com.]

bonded particles, the simple linear contact model is mostly used because it naturally incorporates tensile forces and is computationally efficient.[23,30]

Motion equations

The motion of a single particle is determined by the resultant force and moment vectors acting upon it. Particle motion can be divided into translational and rotational motion. For each particle, the equations of motion can be expressed as two vector equations, the first relating resultant force to the translational motion

$$m\ddot{\mathbf{x}} + \mathbf{F}^{\text{int}} = \mathbf{F}^{\text{ext}} \tag{9}$$

and the second resultant moment to rotational motion

$$\mathrm{I}\ddot{\boldsymbol{\theta}} + \mathbf{M}^{\text{int}} = \mathbf{M}^{\text{ext}} \tag{10}$$

Here, $\mathbf{x}$ and θ are translational and angular position vectors of the particle, respectively; the double dots denotes a second time derivative; and m and I are mass and moment of inertia, respectively (both scalar for spherical particle). $\mathbf{F}^{\text{int}}$ denotes internal forces at the particle contacts; $\mathbf{F}^{\text{ext}}$ stands for external forces, for example, gravitational force, and will be used for capillary forces from the fluid phase. $\mathbf{M}^{\text{int}}$ and $\mathbf{M}^{\text{ext}}$ are the internal and external moment (both in Nm) acting on the particle, respectively. In our case, $\mathbf{M}^{\text{ext}}$ is set to zero, no moment being induced by capillary forces.

Computing particle motion

In DEM calculation, one mechanical time step is as follows. First, particle positions and velocities are initialized. Once neighbors are determined, contacts between particles are identified (which is the most time-consuming procedure) and contact forces computed for touching particles. Then, particle forces and moments are updated including potential external forces and moments. The particle accelerations hence can be computed and the magnitudes of particle velocities and displacements can be integrated. These computations are adopted for each particle in every time step. If the external forces change, many such mechanical time steps are necessary to track the evolution of the particle system. Time-stepping is stopped when particles reach a mechanical equilibrium state. Concerning the present application of DEM to aggregates, one should keep in mind that particle displacements are typically very small, often corresponding to only a tiny fraction of particle diameter.

Bonding models

DEM allows proximate particles to be bonded together by using contact and parallel bond models.[30] The contact bond model extends the linear contact response to particle configurations with negative overlap. This is achieved by simple continuation of the response curve: the contact force is computed by (5) even for negative values of U_{ij}^{n}, up to a predefined maximum force $F_{ij}^{n,\max}$ beyond which the bond breaks and contact force is set to zero. This "breakage of the bond" is interpreted as a normal crack. In shear direction, if the magnitude of the contact force computed by (8) equals or exceeds a prescribed maximum shear contact force $F_{ij}^{s,\max}$, the bond breaks, and the contact force is set to the friction limit $F_{ij}^{s,\max} = \mu_{ij}|\mathbf{F}_{ij}^{n}|$, where μ_{ij} is the friction coefficient of the contact. We will use the contact bond model to describe shrinkage of soft material.

A parallel bond can be envisioned as a set of elastic springs uniformly distributed over a circular cross-section lying on the contact plane and centered at the contact. Unlike the contact bond, the parallel bond can be associated to a physical solid bridge between particles, as in a real aggregate. Parallel bonds establish an elastic interaction between particles that acts in parallel to the particle-based portion of the force-displacement behavior. Thus, the existence of a parallel bond does not totally prevent slip. Parallel bonds can transmit both force and moment between particles, whereas particles can transmit only force. Relative motion at a contact causes a force and a moment to develop within the bond as a result of the parallel bond stiffnesses (see Figure 3). The force and moment that act on the two bonded particles are related to the maximum normal and shear stresses acting within the bond. If either of these maximum stresses reaches the corresponding bond strength, that is, cracking threshold, the parallel bond breaks and its contributions to force and moment are no longer considered. We will use the parallel bond model to describe cracks in stiff material.

Model parameters

The physical meaning of the micromechanical properties in DEM, such as normal and shear particle stiffness, that is, K^{n} and K^{s}, is not yet completely understood. So far, two common strategies are used to estimate these crucial model

parameters[30]: For the general case of arbitrary packings of arbitrarily sized particles, model parameters are found by means of a calibration process, in which a particular instance of a model with a particular packing arrangement and set of model parameters is used to simulate a set of material tests (e.g., unconfined compression test, three-point bend test, Brazilian test, etc.). The model parameters are then chosen to reproduce the relevant material properties as measured in such tests. For simple packing arrangements, the relation between model parameters and commonly measured material properties is known a priori.[30] As an example, for a cubic array of spheres with radius R, the apparent Young's modulus can be expressed as $E = \frac{K^n}{4R}$. In this work, the goal has not been to find the micromechanical properties from own experiments; instead, we have used calibration results from literature where available, and known micro-macro relations otherwise.

Currently, a growing research activity can be observed to supply DEM models with parameters obtained from advanced microscale experiments, for example, atomic force microscopy or nanoindentation,[31,32] which directly investigate particle-particle interactions.

Coupling of Pore Network with DEM

Representation of porous structure

We have used the two aforementioned discrete approaches to describe the porous structure. The solid phase is represented by a cubic packing of monosized particles bonded at their contact points (see Figure 4a). Accordingly, void space is represented by a cubic network of cylindrical pores. The radii of these pores, however, have been randomized (with a small standard deviation) to produce the typical capillary effects. Therefore, the two networks are not complementary in a strict sense. Figure 4b shows a network that is partially saturated by a single-component liquid. (For better visualization of differences in pore radii, they are scaled exponentially in the graphical representation.) Throughout the article light gray space (inside pores) represents the air and vapor phase, and dark blue stands for liquid. All simulations start with networks fully saturated with water and drying from the top (at 20°C and atmospheric pressure).

Model coupling scheme

The coupling of the two models (see Figure 4c) is via capillary forces on the particles, which depend on liquid saturation in the pore network and thus change over time. For such a coupled simulation, we compute in a first pass the evolution of pore saturations in a given pore network and the capillary forces as described in the next section. These forces are stored over time in the capillary force protocol. In the second pass, the capillary forces are consecutively applied to the complementary particle network (with its given material properties) to compute the response using DEM. The coupling is one-way, and pore sizes are not updated with changing particle positions. However, for the considered stiff aggregates, the actual change in network geometry because of capillary forces can be neglected. More important than shrinkage are the exerted forces and the resulting cracks. (The case of soft aggregates that exhibit considerable shrinkage will be discussed later.)

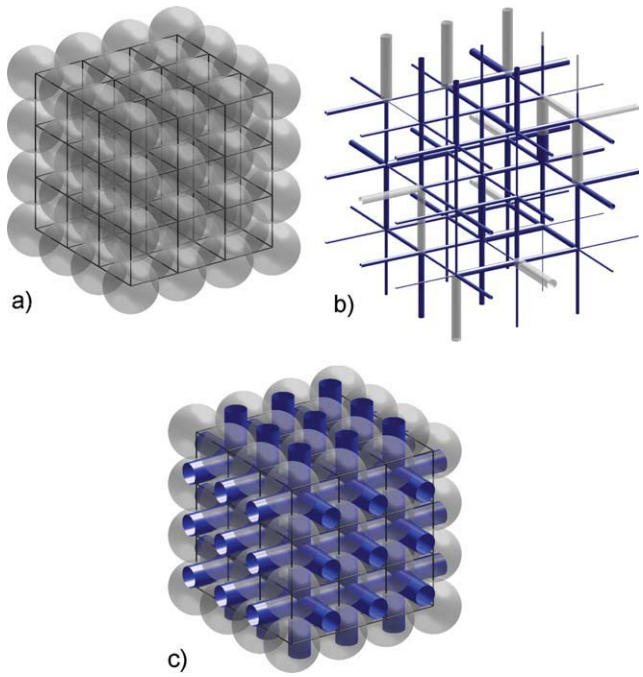

Figure 4. Model porous medium where (a) represents solid phase (bonds are represented as lines), (b) complementary pore network (liquid is plotted in dark blue, gas in light gray), and (c) both networks.

[Color figure can be viewed in the online issue, which is available at wileyonlinelibrary.com.]

As mass transfer is much slower than the mechanical response, for every drying time step, a new (and only slightly different) quasistatic equilibrium is approached in a limited number of mechanical DEM time steps (500); the equilibrium condition is checked by monitoring the mean unbalanced force on the particles, which must tend to zero. Interparticle bond breakage is recorded during simulations to obtain spatial and temporal information on cracks and contact forces.

Capillary forces on particle network

Capillary forces are commonly encountered in nature[33] during processes, such as evaporation and condensation, leading to the formation of liquid bridges with menisci at the liquid-gas interfaces. The surface curvature of the meniscus determines the negative Young–Laplace pressure inside the liquid. This pressure acts in the direction normal to the liquid-solid interface and pulls the solid together. Additionally, there is the direct action of the liquid surface tension, which pulls the contact line of meniscus and solid in the direction of the tangent to the liquid interface. In modeling of the capillary force, many expressions ranging from binary systems—for instance, plate-sphere and sphere-sphere[34]—to an arbitrarily shaped granular medium[35] (multiple systems) have already been developed.

In a cubic particle aggregate, every particle is bonded to six neighboring particles and surrounded by 12 pores. The mean radius of the (cylindrical) pores is computed to match the constrictions of pore space between two pore bodies (see

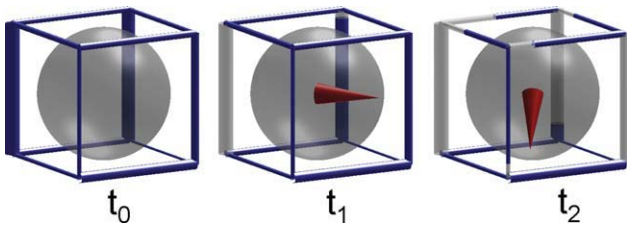

Figure 5. One selected cell of the network with a particle, its neighboring pores and resulting capillary force vector (red cone) as it evolves with pore saturations (liquid in dark blue) during drying.

[Color figure can be viewed in the online issue, which is available at wileyonlinelibrary.com.]

Figure 4c); and the radius of (circular) solid bridges is set to touch those pore cylinders. Therefore, solid phase, that is, primary particles plus solid bridges, and void space are to a certain extent complementary. (Of course, the widening of pores on either side of a constriction is not modeled; furthermore, there is an overlap of the cylindrical pores at the nodes.) The described geometry of pore space justifies that liquid bridges are not modeled because they cannot exist between two neighboring particles, the corresponding space being occupied by solid. Consequently, liquid is considered to be located in the cylindrical pores. However, liquid films[11,12] and—if bonds are not solid—liquid bridges might be subject to future analysis.

Assuming perfect wetting, the capillary force on the particle depicted in Figure 5 depends on effective wet area, A_w, that is, the projection of the wetted area onto a plane perpendicular to the local capillary force, and capillary pressure, $P_c = 2\sigma/r$, in full pores. The mechanical moment that may result from the contribution of the contact line is not considered here. To approximate the capillary force from pore network geometry and pore saturations, we use the following approach. The contributions of all twelve neighboring pores are summed up, where each pore's contribution is a vector directed from particle centre to pore centre (defined as the centre of mass of the full cylindrical pore). For the sake of simplicity, we postulate wet area fractions to be proportional to pore saturations S_j. (Specifically, variations in pore size or capillary pressure are not accounted for.) Thus, for the time-dependent capillary force on each particle, we obtain

$$\mathbf{F}_c(\mathbf{x}_p, t) \propto \sum_{j=1}^{12} S_j(t) \frac{\mathbf{x}_j - \mathbf{x}_p}{|\mathbf{x}_j - \mathbf{x}_p|} \tag{11}$$

where $\mathbf{x}_p$ and $\mathbf{x}_j$ are coordinates of particle centre and pore centers, respectively. In subsequent simulations, we have chosen the proportionality factor in (11) such that capillary pressure in a given network assumes a realistic value and $\mathbf{F}_c$ has the unit of a force.

Evolution of capillary forces during drying

Dynamic simulations are run to see the evolution of capillary forces during drying. In doing so, the aforesaid drying model is applied to the same pore network to investigate the role of liquid phase distributions for mechanical load onto the material. Previous work has shown that phase patterns mainly depend on the relative importance of capillarity and liquid viscosity.[36] Here, the two limiting cases are considered:

1. Liquid viscosity is considered as negligible (for capillary pumping). It must be stressed that this is not only an idealization for liquids with low viscosity but also—and mainly—an approximation of the case that pores are sufficiently large and/or drying rates rather low, so that capillary liquid flow is not affected by friction.
2. Pore liquid is considered as immobile. This case is intended to represent high drying rates and/or drying of small pores, for which viscous effects largely suppress capillary flow. And it can also describe highly viscous liquids such as binder solutions.

Figure 6 shows the respective drying rate curves in dimensionless form. As we are interested in observing the capillary force evolution in the whole system, we generated relatively small networks ($5 \times 5 \times 10$) with particle diameter (and pore length) 500 nm. The boundary layer is 5 μm thin, corresponding to a mass transfer coefficient of 5.1 m/s. Pore radius is normally distributed with 103 nm mean and standard deviation 1 nm. (For the studied system, typical capillary pressure is of the order of 1.4 MPa, and net capillary forces as shown in Figure 5 are in the range of 0.35 μN.) The width of pore size distribution determines the ratio of capillary to viscous effects and therefore plays no major role in the two limiting cases. For drying conditions between the two discussed limits, intermediate behavior is observed as shown in Figure 6 for the case of water. Pore network saturations and capillary forces during the drying process are depicted in Figure 7 for negligible liquid viscosity, whereas the result of the immobile water simulation is presented in Figure 8.

Discussing the capillary force evolution and starting with the nonviscous case, one can see from Figure 7a that in the fully saturated network, capillary forces appear on the top surface as well as on the other surfaces (on which empty

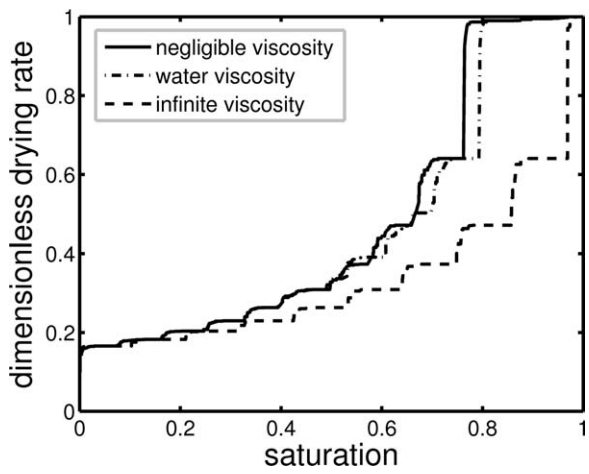

Figure 6. Normalized drying rate vs. network saturation for the simulations depicted in Figures 7 and 8, as well as for the case of water viscosity.

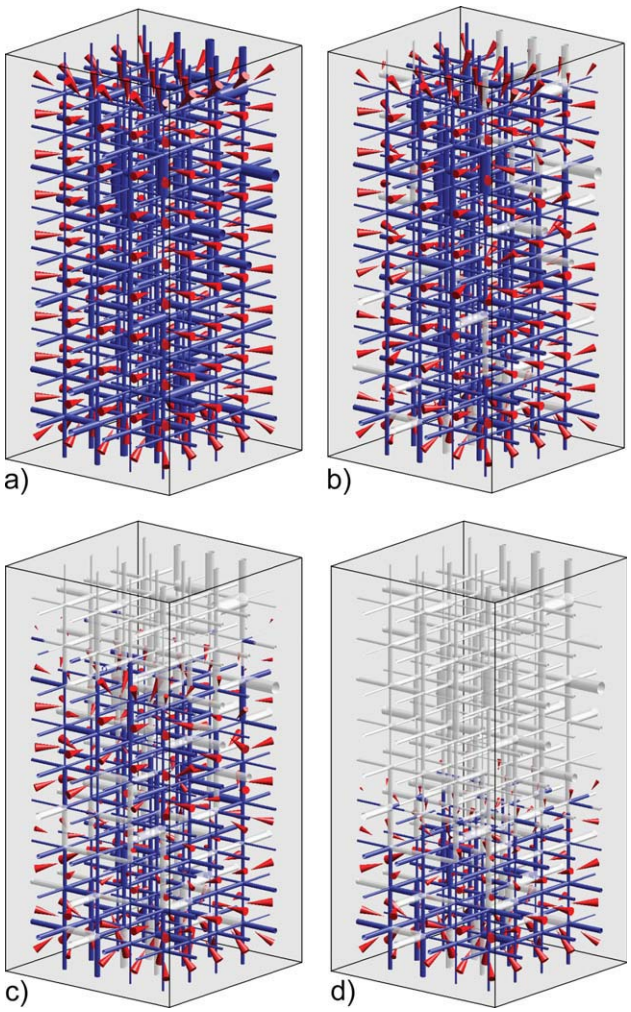

Figure 7. Evolution of capillary forces for negligible liquid viscosity at (a) full saturation and at network saturations, (b) 0.9, (c) 0.6, and (d) 0.3; gray cylinders represent empty pores, and dark blue is for liquid; capillary forces are presented by red cones, and cone size scales with force magnitude.

The network is subjected to evaporation at the top. (For better visualization of differences in pore radii, they are scaled exponentially). [Color figure can be viewed in the online issue, which is available at wileyonlinelibrary.com.]

pores have been imposed). In this regime, the compressive capillary forces are symmetric and the net capillary force on inner particles is zero. As evaporation continues, the liquid phase splits up into small disconnected clusters (Figures 7b, c). Accordingly, capillary forces get less organized such that they are still compressive for the individual clusters whereas, at the local level, tension forces can develop. Globally, capillary forces decline downwards and eventually vanish at the bottom of the network by the end of drying. However, in the high viscosity limit, liquid stays in a single cluster and a sharp drying front propagates through the network, accompanied by a capillary force front that keeps the wet region under compression (Figure 8); therefore, the force gradient in this case is rather significant. At the bottom of the network, the local capillary forces stay constant until this region eventually dries out at the end of the process.

In conclusion, it shall be stressed that—depending on drying conditions—capillary forces evolve in different ways. In the following, the question is addressed whether these capillary interactions may promote mechanical effects and whether these depend on drying conditions.

Evolution of contact force distribution

In this part, we describe the impact of local capillary force evolution during drying on the global bond network. This is demonstrated by a network of contact forces and cracks. Figure 9 represents interparticle contact forces in a small $5 \times 5 \times 10$ particle network with 625 bonds (with material parameters as in Table 1). The resultant contact forces are computed by applying the capillary forces from the previous section (for the high viscosity limit) in Eqs. 4–8. If capillary forces are comparable with bond strength, microcracks may occur. Figure 9a illustrates the situation in the early stage of drying (saturation 0.6), where 4% of the network bonds have broken. We can see that the contact forces are less pronounced in the dried network region because bond failures allow the particles to reorganize and thus relieve the tensile forces in the contact points. As drying progresses to network saturation 0.3, cracks (8% of bonds) propagate downwards resulting in a network that is practically free of tensile forces. These simulation results are in qualitative accord with numerical[4,18] and experimental[37] observations.

To provide a detailed insight into how a microcrack initiates, we have analyzed a normal contact force evolution while applying the capillary forces in two different drying conditions. In fact, we assume in our model that the history of the contact force is not involved in crack formation. Despite the crack being only a result of the current state of the contact force, this force is a result of the emptying order of pores; therefore the drying conditions are crucial. Simulations start with a fully saturated network where the capillary forces are pronounced; and the particles are in mechanical equilibrium state. Figure 10 shows an example of normal contact force evolutions in one specific (vertical) bond near the center of the network for the two limiting drying conditions (see Table 1 for material parameters). Initially, capillary forces cause compression of the particles (positive values of contact force). When the drying front passes the bond, the action changes into tension (negative value of contact force), which may eventually result in the breakage of the bond if the current force reaches bond strength (in the given example, -10.8×10^{-10} N). In the highly viscous limit, the capillary force field in the wet part is rather uniform in lateral directions with a sharp change near the drying front (see Figure 8). In this case, the gas invasion takes time to reach the bond and the bond experiences strong local compression for longer. In the nonviscous case, pores are invaded throughout the network leading to a disordered capillary force field, and a weakening of normal compressive contact force in the partially saturated region (at saturation 0.88). A preliminary analysis of these two different behaviors at the sample scale is done in the next section.

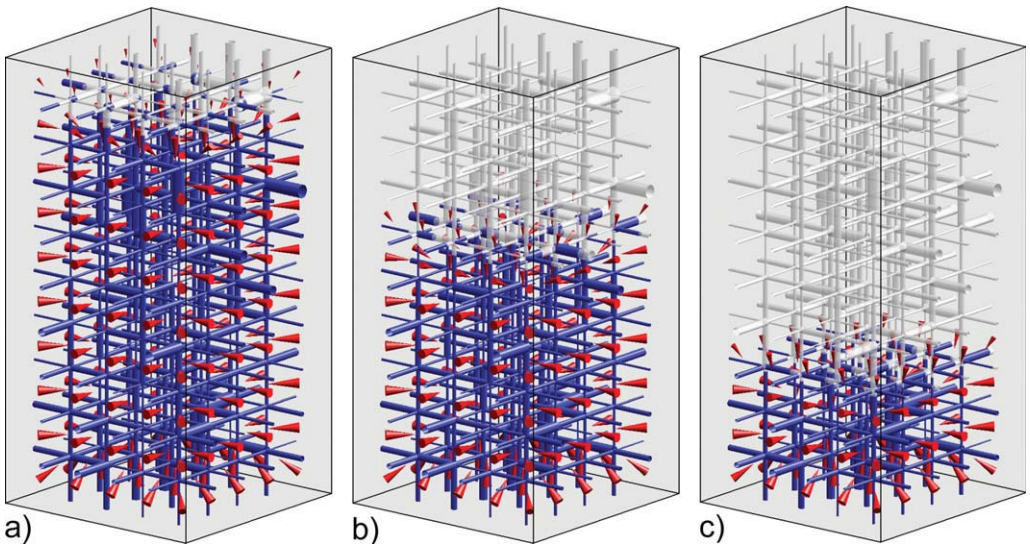

Figure 8. Evolution of capillary forces for immobile water at network saturations (a) 0.9, (b) 0.6, and (c) 0.3; gray cylinders represent empty pores, and dark blue is for liquid; capillary forces are presented by red cones, and cone size scales with force magnitude.

The network is subjected to evaporation at the top. (For better visualization of differences in pore radii, they are scaled exponentially). [Color figure can be viewed in the online issue, which is available at wileyonlinelibrary.com.]

Simulation of Cracks and Shrinkage During Drying

In practice, damage by cracks is rather observed during drying of stiff materials (with high elastic modulus), whereas shrinkage is the main effect when soft materials (with low elastic modulus) are dried. In the DEM approach, the terms "stiff" and "soft" are translated into the behavior of primary particle contacts, for example, soft particles can have significant virtual overlap. (We restrict our analysis to elastic behavior, which is no general constraint to the method.) In this section, we present numerical results for different drying conditions as well as for both types of materials to show these phenomena. Such simulations shall in future help to find criteria for material properties and drying conditions to preserve the solid structure. At first, we use a relatively small network for qualitative discussion of phenomena; later on, larger networks aim at more representative results.

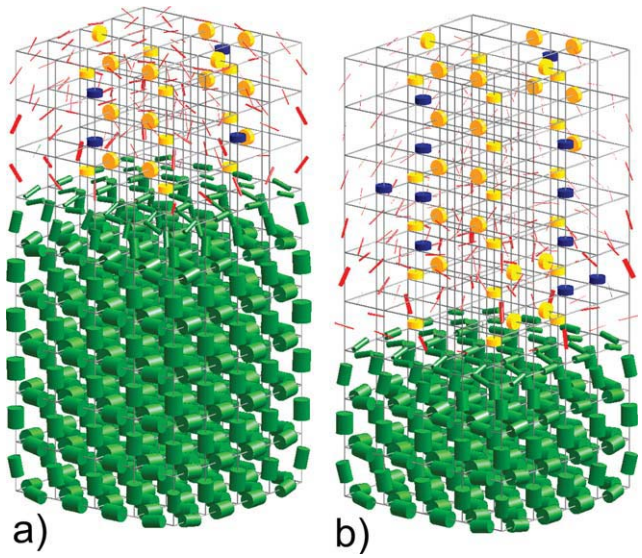

Figure 9. Contact force distributions and crack developments at network saturations (a) 0.6 and (b) 0.3. Compressive and tensile contact forces are represented by green and red cylinders, respectively (radius indicating force magnitude, orientation accounting for normal and shear components).

Normal and shear cracks are visualized by dark blue and yellow discs, respectively. [Color figure can be viewed in the online issue, which is available at wileyonlinelibrary.com.]

Influence of drying conditions

We show how the dynamics of crack formation in stiff particle aggregates is influenced by drying conditions. To this purpose, we have chosen microparameters for a rather dense porous agglomerate, namely activated alumina γ-Al_2O_3 (as used in[23]); as particle radii are about two orders of magnitude smaller in our work, we have scaled parallel bond stiffness accordingly (to get similar values in units N/m). For simplicity, a uniform bond radius has been used,

Table 1. Microparameters of Stiff Particle Networks

Characteristic	Value
Particle radius (m)	250×10^{-9}
Particle density (kg/m^3)	3230
Friction coefficient between particles	0.5
Damping ratio	0.7
Normal/shear stiffness of particles (N/m)	3×10^4
Normal/shear stiffness of parallel bonds (N/m^3)	8×10^{14}
Normal/shear strength of parallel bonds (N/m^2)	1.6×10^4
Bond radius (fraction of particle radius)	0.5858

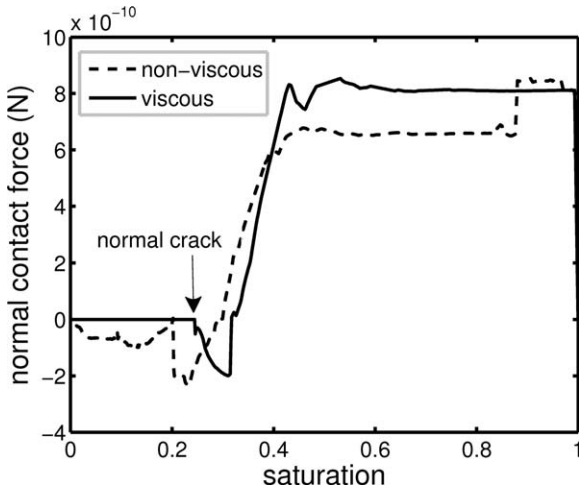

Figure 10. Evolution of normal contact forces at one specific contact in nonviscous and highly viscous limit.

which is computed from interparticle distances and mean pore radius as explained above.

First, we analyze the case of negligible liquid viscosity: capillary flow and resulting liquid phase distributions have been discussed in context with Figure 7. In a second simulation step, the capillary forces corresponding to these phase distributions have been applied to the stiff particle aggregate; the resulting normal and shear cracks of bonds are shown in Figure 11.

At high network saturations, when the network as a whole loses liquid but stays partially saturated to the surface (first drying period), it remains under compression by capillary forces. During this initial period, only shear cracks are observed, their number rising with drying time. At later stages of drying, the drying front recedes and a completely dry region develops (second drying period). This dry region is no longer under compression because of the absence of capillary forces. Therefore, also normal cracks may occur. In this second period, normal cracks gradually appear as the dry region moves into the network; and also more shear cracks occur in the vicinity of the drying front. At the end of drying, 66 shear cracks and 15 normal cracks are counted, that is, 81 out of 625 bonds have broken. These cracks are not uniformly distributed in space: the decrease of cracks from top to bottom of the sample is attributed to the nonsymmetric force load on the different regions.

If liquid is immobile, all surface pores dry out immediately and a sharp drying front recedes into the pore network as shown in Figure 8. The mechanical response of the solid network is presented in Figure 12. At the beginning, the bottom of the network stays completely saturated, and therefore, experiences no changes in capillary forces, no cracks are observed in that region. Only in the vicinity of the receding phase front, cracks occur. As argued for the nonviscous case, normal cracks may only occur in the dry region where the network is no longer under compression. In this way, together with the propagating drying front, a crack front moves towards the bottom of the network, resulting in a total of 42 shear cracks and 12 normal cracks. This means that 54 out of 625 bonds have failed during the drying process. These final numbers are very similar to those of the nonviscous case. The main difference seems to be in the time-dependence of crack appearance, because cracks only occur in the neighborhood of local changes in liquid saturation.

Influence of bond strength

To show the future potential of this modeling approach, bond strength has been systematically varied to determine its effect on crack formation and distribution. To this purpose, a nonviscous drying simulation has been used with the same pore and particle network parameters as before (see Table 1). As shown in Figure 13 and Table 2, by increasing bond strength, the total number of cracks can be reduced. This is

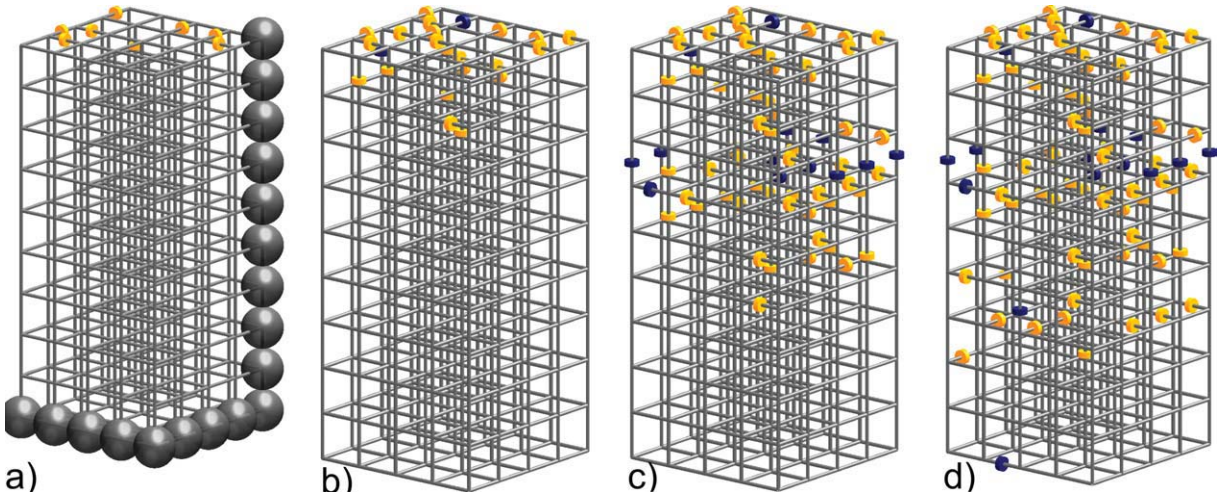

Figure 11. Distribution of microcracks for negligible liquid viscosity at network saturations (a) 0.9, (b) 0.6, and (c) 0.3 as well as (d) for the completely dry aggregate.

Dark blue and yellow cylinders stand for normal and shear cracks, respectively. (For better readability, only the bond network is shown.). [Color figure can be viewed in the online issue, which is available at wileyonlinelibrary.com.]

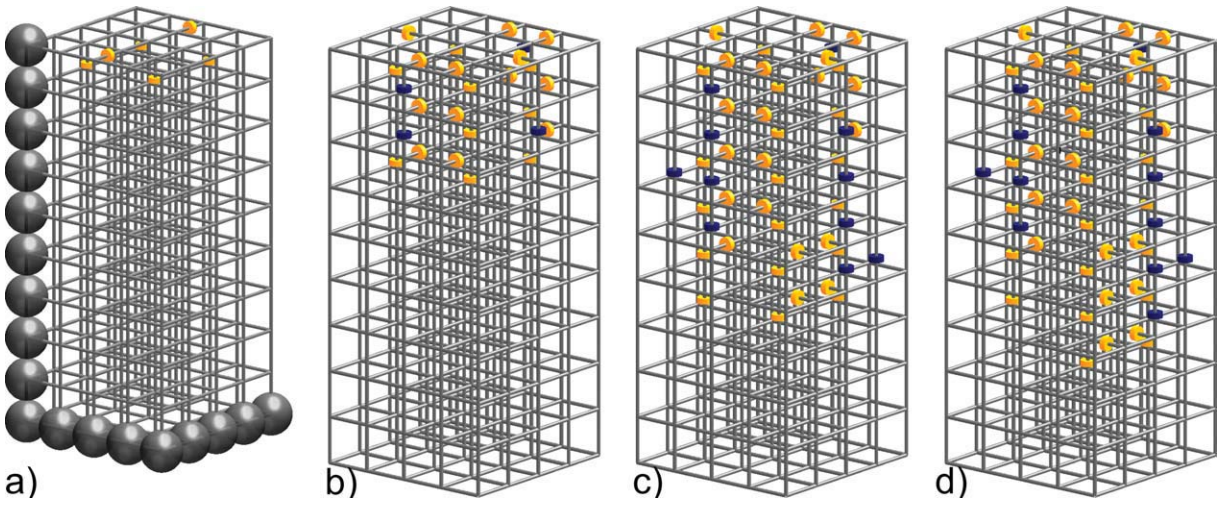

Figure 12. Distribution of microcracks for immobile liquid at network saturations (a) 0.9,(b) 0.6, (c) 0.3, and (d) for the completely dry aggregate.

Dark blue and yellow cylinders stand for normal and shear cracks, respectively. [Color figure can be viewed in the online issue, which is available at wileyonlinelibrary.com.]

clear as the bonds can better withstand the capillary forces occurring during drying. As a second effect, the type of cracks is changed: for higher bond strength, shear cracks are dominating, whereas the numbers of normal and shear cracks are comparable for weak bonds. Moreover, the time-dependency of the process can be observed, and influence of the bond strength on the number of cracks seems to be stronger in the second drying period than in the first. In the first drying period, when liquid is removed from the whole network, mainly shear cracks may occur. In the second period, when the drying front recedes (here at network saturation <0.75), still intact bonds may be broken by additional shear cracks and also normal cracks. This means that cracks occur to a great extend in the second drying period.

Monte-Carlo simulations

In the previous parts, only one realization of the network structure in each drying condition was considered; simulation results showed slightly more cracks for the nonviscous limit of drying. To push the analysis further and being aware of the fact that randomness of network generation may lead to quite different network saturation distributions and accordingly varied mechanical responses, Monte-Carlo simulations on larger networks have to be run. Present computational cost and memory limitations impose a relatively small particle network size ($10 \times 10 \times 20$, corresponding to 5500 interparticle bonds) and a limited number (10) of MC simulations per drying condition. Simulations are carried out with the same pore and particle parameters as above (see Table 1).

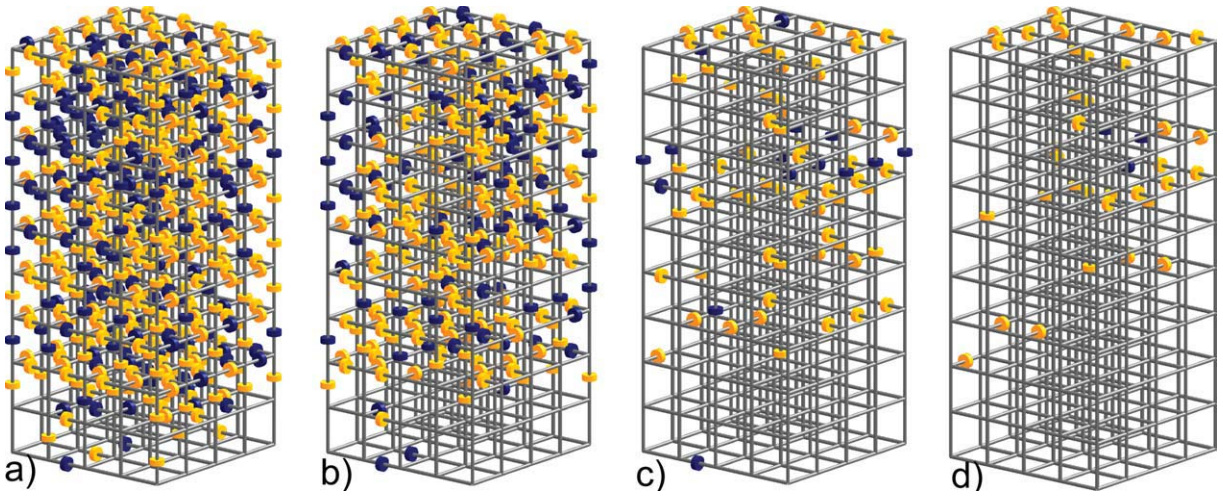

Figure 13. Cracks at the end of drying of brittle aggregates for different bond strengths when liquid viscosity is neglected (see Table 2 for numbers).

[Color figure can be viewed in the online issue, which is available at wileyonlinelibrary.com.]

Table 2. Stiff Aggregate Behavior for Varying Bond Strength

	a	b	c	d
Normal and shear bond strength (10^4 N/m^2)	0.4	0.8	1.6	2
Number of cracks during first drying period				
Shear	52	23	13	10
Normal	13	14	2	0
Total	65	37	15	10
Number of cracks during second drying period				
Shear	290	197	53	26
Normal	162	90	13	3
Total	452	287	66	29
Total number of cracks	517	324	81	39

Simulations results are summarized in Table 3 as average numbers of cracks with respective statistical standard deviations. First, one can notice a size effect: for the same micromechanical parameters as above, the fraction of broken bonds is considerably larger for this larger network. Second, the results indicate that more normal cracks, but less shear cracks have occurred in the viscous limit than in the nonviscous. These two opposing effects compensate each other and the discrepancy in total number of cracks is not significant. In other words, in both cases, the order of emptying the pores is different, but a representative bond experiences—sooner or later in the drying process—similar local tensions, which mainly occur when its direct-neighbor pores are emptied. Regarding the spatial distributions of cracks, very regular crack patterns are obtained for the viscous limit, whereas the nonviscous limit produces correlated, but irregular crack patterns (not shown).

In reality, the liquid pressure in the pores has a gradient that depends on drying rate; this gradient is expected to be negligible in the nonviscous limit and to be pronounced for the viscous limit. As discussed in literature,[18] this pressure gradient leads to tensile forces near the evaporating surface and the combination of macroscopic tension and local ''switching off'' of capillary forces is expected to result in macroscopic cracks. Such differences in liquid pressures are not yet included in the modeling of forces, so that cracks are only described on a ''local'' basis.

Shrinkage for soft materials

At last, an application of the new method to soft materials is outlined. One prominent example is highly porous gels that show considerable—and sometimes reversible—shrinkage during drying. To our knowledge, no DEM simulation of such materials has yet been performed, so that in the lack of literature parameters, we use the simple linear contact bond model with parameters (see Table 4) that correspond to typical macroscopic moduli. It is not evident that the mechanisms during elastic compaction of a gel matrix, that is, the reversible folding of solid filaments, can be approximated by overlapping of soft discrete particles. Indeed, the particles in DEM simulation now rather represent small portions of solid material than real primary particles, and the liquid distribution in the pore network is an averaged one. Nevertheless, we will see that qualitative effects can be correctly reproduced by the chosen DEM approach. Contact force distribution during shrinkage is shown in Figure 14 for a $10 \times 5 \times 5$ network. Initially, the aggregate is in mechanical equilibrium and capillary forces are not yet loaded (Figure 14a). Then, in one step, the full capillary forces are applied to the aggregate leading to a new equilibrium between attractive capillary and repulsive contact forces with considerable shrinkage (Figure 14b). In fact, this single step corresponds to a complete first drying period during which liquid removal is compensated by ideal shrinkage, that is, all pores remain fully saturated but reduce their size. The kinetics of this period are not yet modeled; specifically, volume change of pores is not accounted for and viscous effects leading to nonuniform shrinkage (or even a ''premature'' end of the first drying period by emptying of pores) are not yet addressed. Therefore, we restrict ourselves to the nonviscous limit, where uniform shrinkage can be assumed.

As evaporation continues in the second drying period, capillary forces gradually disappear from the top and repulsive contact forces bring the particles back to their initial positions (see Figure 14c). Such a spring-back phenomenon is known to occur for certain gels.[38,39] Eventually, mechanical equilibrium for the dried aggregate will be reached, without cracks having occurred. A near equilibrium state is shown in Figure 14d. In the second period, the results are meaningful even if volume change is neglected, because it concerns the gas pores, which play a minor role in transport phenomena.

Table 3. Number Distributions of Cracks for 10 MC Runs of Nonviscous and Viscous Drying

	Nonviscous	Viscous
Normal cracks	1245 ± 57	1490 ± 20
Shear cracks	1660 ± 50	1350 ± 29
Total cracks	2900 ± 36	2850 ± 39

Conclusions

A discrete approach has been presented to model mechanical effects during isothermal drying of porous materials. The solid phase is represented by a particle network, the void space by a complementary pore network. Local capillary forces are computed from pore saturations as obtained from

Table 4. Microparameters of Soft Particle Networks

Characteristic	Value
Particle radius (m)	250×10^{-9}
Particle density (kg/m^3)	2000
Friction coefficient between particles	0.5
Normal/shear stiffness of particles (N/m)	10
Normal/shear contact bond strength/capillary force	2

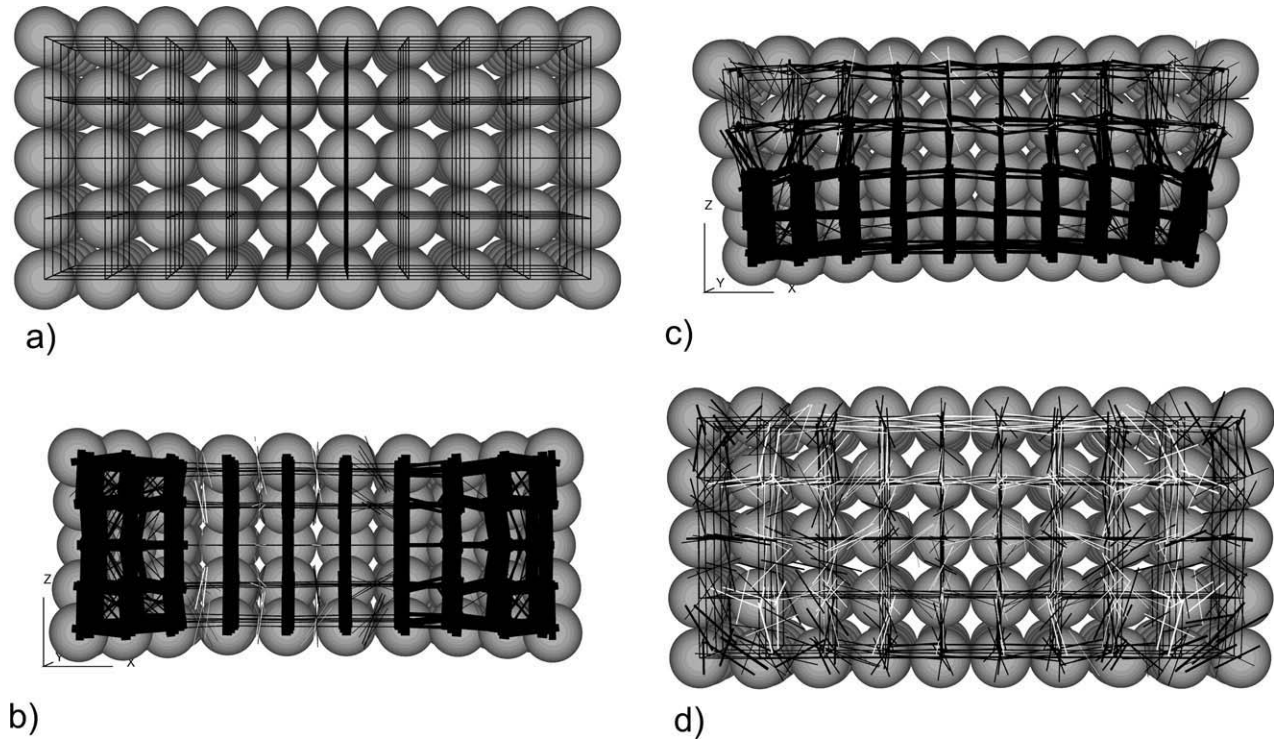

Figure 14. Volumetric shrinkage and contact force distribution of a soft aggregate at four different times during drying: (line thickness indicates relative force; black color means compression and white tension).

a pore network drying algorithm and then applied to the particle network by use of DEM.

For soft materials, such as gels, spring-back of the material, which has shrunken during the first drying period, has been described. For stiff materials, influence of liquid phase distributions during drying and material properties on material response (i.e., the occurrence of cracks) has been investigated. Our results suggest that different spatial distributions of liquid and resulting capillary forces during drying cannot explain the fact that faster drying leads to greater material damage. Instead, our simulations seem to confirm the hypothesis that only the combination of local forces and macroscopic stress leads to this damage.[18]

Although the current model version is still limited, the presented results correctly describe material behavior at a qualitative level. By this, the aptitude of the discrete approach to describe drying phenomena has been demonstrated; and appropriate model extensions are believed to make the model predictive. For example, two-way coupling shall be introduced by accounting for shrinkage in the pore network. Another major effect is the pressure gradient[18] in the liquid, which causes differential stress and nonuniform shrinkage of the solid. A model extension accounting for exact liquid pressures is expected to allow the simulation of differential stress in the solid and of (propagating) macrocracks. Further, the approach may be extended to nonisothermal effects, which are already included in PNMs. Ongoing research work extends the presented model to irregular particle aggregates and their complementary pore networks. Additionally, DEM offers the possibility to use more complex contact and particle properties. Advanced microscale experiments will allow parameterization of the DEM model, and analysis of damaged dry material will help assess simulation results for cracks in a more rigorous way.

In conclusion, the presented technique is seen as a new powerful tool to analyze interactions between fluid and solid phases during drying at the pore level. In this approach, as microscopic behavior can be directly investigated, truly local information is available from simulations (as opposed to continuous models). Indeed, such modeling efforts are undertaken in the belief that discrete approaches to classical problems can help for a fundamental understanding and that more refined model versions will allow studying mechanical effects for a wide range of materials and drying conditions.

Acknowledgments

This work was financed by the German Research Foundation (DFG) in the frame of Graduate School 828 "Micro-Macro-Interactions in Structured Media and Particulate Systems".

Literature Cited

1. Lewis RW, Strada M, Comini G. Drying-induced stresses in porous bodies. *Int J Numer Methods Eng*. 1977;11:1175–1184.
2. Kowalski SJ. *Thermomechanics of Drying Processes*. Berlin: Springer, 2003.
3. Job N, Sabatier F, Pirard JP, Crine M, Léonard A. Towards the production of carbon xerogel monoliths by optimizing convective drying conditions. *Carbon*. 2006;44:2534–2542.
4. Pourcel F, Jomaa W, Puiggali JR, Rouleau L. Criterion for crack initiation during drying: alumina porous ceramic strength improvement. *Powder Technol*. 2007;172:120–127.
5. Katekawa ME, Silva MA. A review of drying models including shrinkage effects. *Drying Technol*. 2006;24:5–20.

6. Prat M. Percolation model of drying under isothermal conditions. *Int J Multiphase Flow*. 1993;46:691–704.
7. Nowicki SC, Davis HT, Scriven LE. Microscopic determination of transport parameters in drying porous media. *Drying Technol*. 1992;10:925–946.
8. Yiotis AG, Stubos AK, Boudouvis AG, Yortsos YC. A 2-D pore network model of the drying of single-component liquids in porous media. *Adv Water Resour*. 2001;24:439–460.
9. Laurindo JB, Prat M. Modeling of drying in capillary-porous media: a discrete approach. *Drying Technol*. 1998;16:1769–1787.
10. Metzger T, Irawan A, Tsotsas E. Isothermal drying of pore networks: influence of friction for different pore structures. *Drying Technol*. 2007;25:49–57.
11. Yiotis AG, Boudouvis AG, Stubos AK, Tsimpanogiannis IN, Yortsos YC. The effect of liquid films on the drying of porous media. *AIChE J*. 2004;50:2721–2737.
12. Prat M. On the influence of pore shape, contact angle and film flows on drying of capillary porous media. *Int J Heat Mass Transfer*. 2007;50:1455–1468.
13. Huinink HP, Pel L, Michels MAJ, Prat M. Drying processes in the presence of temperature gradients, pores scale modeling. *Eur Phys JE*. 2002;9:487–498.
14. Plourde F, Prat M. Pore network simulations of drying of capillary media. Influence of thermal gradients. *Int J Heat Mass Transfer*. 2003;46:1293–1307.
15. Surasani VK, Metzger T, Tsotsas E. Consideration of heat transfer in pore network modeling of convective drying. *Int J Heat Mass Transfer*. 2008;51:2506–2518.
16. Segura LA, Toledo PG. Pore-level modeling of isothermal drying of pore networks. Effects of gravity and pore shape and size distributions. *Chem Eng J*. 2005;111:237–252.
17. Metzger T, Irawan A, Tsotsas E. Influence of pore structure on drying kinetics: a pore network study. *AIChE J*. 2007;53:3029–3041.
18. Brinker CJ, Scherer GW. *Sol-Gel Science*. New York: Academic Press, 1990.
19. Amaral M. Deformation of solid surface due to capillary forces. *J Colloid Interface Sci*. 1984;100:17–26.
20. Segura L, Toledo PG. Pore-level modeling of isothermal drying of pore networks accounting for evaporation, viscous flow, and shrinking. *Drying Technol*. 2005;23:2007–2019.
21. Cundall PA, Strack ODL. A discrete numerical model for granular assemblies. *Geotechnique*. 1979;29:47–65.
22. Moreno-Atanasio R, Ghadiri M. Mechanistic analysis and computer simulation of impact breakage of agglomerates: effect of surface energy. *Chem Eng Sci*. 2006;61:2476–2481.
23. Antonyuk S. *Deformations- und Bruchverhalten von kugelförmigen Granulaten bei Druck- und Stoßbeanspruchung*, PhD thesis. Otto-von-Guericke-Universität, Magdeburg; 2006.
24. Richefeu V, Youssoufi MSEI, Radjaï F. Shear strength properties of wet granular materials. *Phys Rev E*. 2006;73:051304–11.
25. Scholtès L, Chareyre B, Nicot F, Darve F. Micromechanics of granular materials with capillary effects. *Int J Eng Sci*. 2009;47:64–75.
26. Jintang L, David JM. Application of the discrete element modeling in air drying of particulate solids. *Drying Technol*. 2002;20:255–282.
27. Kharaghani A. *Irregular Pore Networks and Mechanical Effects During Drying of Porous Media*, PhD thesis. Otto-von-Guericke-Universität, Magdeburg; 2010.
28. Irawan A. *Isothermal Drying of Pore networks: Influence of Pore Structure on Drying Kinetics*, PhD thesis. Otto-von-Guericke-Universität, Magdeburg; 2006.
29. Cundall PA. A computer model for simulating progressive, large scale movements in blocky rock systems. *Proc Symp Int Soc Rock Mech. Nancy*. 1971;1:129–136.
30. Itasca Consulting Group Inc. Particle Flow Code in Three-Dimension Manual, Version 3.10 (2005), Itasca Consulting Group Inc., Minneapolis, Mn, USA.
31. Tykhoniuk R, Tomas J, Luding S, Kappl M, Heim L, Butt HJ. Ultrafine cohesive powders: from interparticle contacts to continuum behavior. *Chem Eng Sci*. 2007;62:2843–2864.
32. Dutta AK, Penumadu D. Hardness and modulus of individual sand particles using nanoindentation. *Geotech Special Publication*. 2007;173:34–43.
33. Young T. An essay on the cohesion of fluids. *Phil Trans R Soc Lond*. 1805;95:65–87.
34. Rabinovich YI, Esayanur MS, Moudgil BM. Capillary forces between two spheres with a fixed volume liquid bridge: theory and experiment. *Langmuir*. 2005;21:10992–10997.
35. Grof Z, Lawrence J, František S. Computer simulation of evolving capillary bridges in granular media. *Granular Matter*. 2008;10:93–103.
36. Metzger T, Tsotsas E. Viscous stabilization of drying front: three-dimensional pore network simulations. *Chem Eng Res Des*. 2008;86:739–744.
37. Bisschop J, van Mier GM. Effects of aggregates on drying shrinkage micro-cracking in cement-based composites. *Mater Struct*. 2002;35:453–461.
38. Dong H, Reidy RF, Brennan JD. Shrinkage and springback behavior of Methylsilsesquioxanes prepared by an acid/base two-step processing procedure. *Chem Mater*. 2005;17:6012–6017.
39. Hwang SW, Jung HH, Hyun SH, Ahn YS. Effective preparation of crack-free silica aerogels via ambient drying. *J Sol-Gel Sci Tech*. 2007;41:139–146.

Manuscript received Aug. 17, 2009, and revision received May 15, 2010.